THE JOURNAL OF PHYSICAL CHEMISTRY C
A JOURNAL OF THE AMERICAN CHEMICAL SOCIETY

pubs.acs.org/JPCC

Article

Ion Conductivity in a Magnesium Borohydride Ammonia Borane Solid-State Electrolyte

Mauro Palumbo,* Kazuaki Kisu, Valerio Gulino, Carlo Nervi, Lorenzo Maschio,* Silvia Casassa, Shin-ichi Orimo, and Marcello Baricco

Cite This: *J. Phys. Chem. C* 2022, 126, 15118−15127

Read Online

ACCESS | Metrics & More | Article Recommendations | Supporting Information

ABSTRACT: Due to the high cost and limited availability of lithium, Mg-based batteries are currently being investigated as a promising alternative. A critical component in these batteries is the electrolyte, with all-solid-state ones that show superior safety features but must guarantee adequate ionic conductivity to be viable for applications. In this work, a metal borohydride ammonia borane complex, $Mg(BH_4)_2(NH_3BH_3)_2$, was theoretically investigated using state-of-the-art ab initio methods based on density functional theory (DFT) approaches and software for the modeling of battery materials. Several features of this compound were first characterized, including its crystal structure and topology, vibrational properties, and infrared and Raman spectra. Theoretical results were compared with experiments showing excellent agreement, thus properly setting the ground for ionic transport analysis. Magnesium ion migration was then investigated by performing climbing image nudged elastic band (CI-NEB) calculations. The most promising migration path occurs along the c-axis and presents two transition states with a calculated migration barrier (including weak van der Waals interactions) in the range of 0.550−0.668 eV. The topological analysis suggests repulsive interactions between Mg and B atoms. It has been confirmed that defect formation energy plays an essential role in correctly evaluating the activation energy for ion migration, as shown by comparing calculated and experimental results for this system. Assuming the formation of Frenkel pairs as the dominant mechanism, the calculated defect formation energy is 1.05 eV (per single defect), which combined with the migration barrier gives a value of the activation energy for migration in the range of 1.60−1.71 eV. The present findings confirm that the activation energy for ion migration in solid-state electrolytes can be reliably estimated by DFT-based methods.

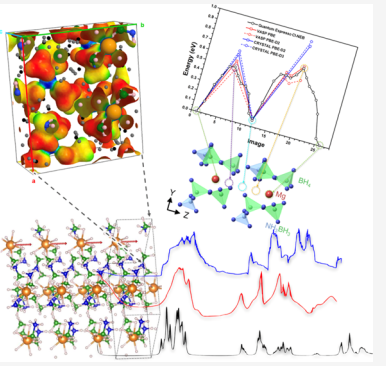

1. INTRODUCTION

The increasing global demand for renewable energy and energy storage devices is driving the ongoing research for better materials for batteries.[1,2] Li-ion-based devices are already widely used, but alternative materials based on Mg ions have been proposed for the new generation of all-solid-state batteries.[3−9] The substitution of Li with Mg is both safer and cheaper, as they are not flammable or subject to exploding and have a larger theoretical capacity, thanks to the double charge per ion.[10,11] Despite the higher molecular mass, the use of Mg electrodes is also advantageous compared to Li ones, as these anodes have high volumetric capacity and good redox potential and magnesium is more abundant than lithium.[12] However, significant challenges have been faced in finding a suitable solid-state electrolyte exhibiting both high ionic conductivity and good oxidative/reductive stability.[13,14] New ad-hoc electrolytes need, therefore, to be developed, and inorganic solid-state ionic conductors could be viable candidates because they are intrinsically safer than liquids.[15,16] The bivalent nature of Mg ions however represents a significant obstacle to their mobility, and high values of ionic conductivity have been proved elusive for these materials.[17] Recently, complex hydride materials based on $Mg(BH_4)_2$ have received particular attention as they have shown relatively high conductivities.[18−22] A very recent promising candidate has been found to be magnesium borohydride ammonia borane, $Mg(BH_4)_2(NH_3BH_3)_2$, which has shown an ionic conductivity of 1.3×10^{-5} S cm^{-1} at 30 °C.[23] Furthermore, from the measured temperature dependence of the ionic conductivity, an activation energy of 1.47 eV has been estimated. The higher conductivity in this system, compared to $Mg(BH_4)_2$, has been attributed to the larger Mg−B bond length and volume of the tetrahedron surrounding Mg atoms, as a result of the substitution of two borohydrides $[BH_4]^-$ with two ammonia borane $[NH_3BH_3]$.

The temperature dependence of ionic conductivity σ is related to the activation energy (E_A) according to ref 24

Received: July 12, 2022
Revised: August 16, 2022
Published: August 30, 2022

Table 1. Calculated and Experimental Lattice Parameters of Magnesium Borohydride Ammonia Borane $Mg(BH_4)_2(NH_3BH_3)_2$

	a (Å)	b (Å)	c (Å)	b/a	c/a	V (Å^3)	ref
experimental	14.4135	13.2084	5.1118	0.916	0.355	973.2	30
experimental	14.41633(7)	13.21283(7)	5.11512(2)	0.916	0.355	974.331(8)	29
experimental	14.45946	13.22299	5.12454	0.914	0.387	979.798	23
calc. QE PBE vdW-DF2	14.2590	13.1615	4.7664	0.9230	0.3343	894.51	this work
calc. VASP PBE-D2	14.0996	13.0998	4.5196	0.929	0.321	834.8	this work
calc. VASP PBE	14.6681	13.2285	5.2925	0.902	0.361	1027.0	this work
calc. CRYSTAL −PBE-D2	14.3042	13.0493	4.6730	0.912	0.327	872.3	this work
calc. CRYSTAL PBE	14.7283	12.9432	5.4834	0.879	0.372	1045.3	this work

$$\sigma = \frac{\sigma_0}{T} e^{-E_A/k_B T} \quad (1)$$

where σ is the ionic conductivity at temperature T, k_B is the Boltzmann constant, and σ_0 is a pre-exponential factor that takes into account ionic charge and concentration, hopping frequency, and geometrical parameters. Equation 1 is used to obtain the activation energy (E_A) from experimental measurements of conductivity at different temperatures. The activation energy (E_A) can be expressed as the sum of two terms

$$E_A = E_m + E_f/2 \quad (2)$$

where E_m is the migration energy barrier and E_f is the energy needed to create the defects, which are necessary for ion migration.[25,26] The migration energy can be calculated from density functional theory (DFT) energies along pathways where the ions can possibly travel.[27,28]

In the present study, we performed a theoretical investigation of magnesium borohydride ammonia borane to gain further insight into ion mobility in this system and to explain recent experimental findings.[23] The crystal structure and the thermodynamic stability of this compound have been investigated using DFT and different computer codes. First, a topological analysis has been carried out to identify and investigate possible migration paths for Mg^{2+} ions. A selected pathway for Mg ions within the $Mg(BH_4)_2(NH_3BH_3)_2$ structure has been further analyzed using DFT, combined with the climbing image nudged elastic band (CI-NEB) method. The formation of defects and the associated energy has finally been calculated using DFT methods to compare theoretical estimations for the activation energy with experimental findings.

2. METHODS

The crystal structure of $Mg(BH_4)_2(NH_3BH_3)_2$ complex hydride has been taken from the literature.[23,29,30] It is an orthorhombic unit cell (space group $P2_12_12_1$) with the c lattice parameter significantly shorter than a and b (Table 1) and with a total of 108 atoms. Two independent borohydride (BH_4^-) groups and two ammonia borane (NH_3BH_3) groups are coordinated with the same Mg atom.

2.1. Topological Analysis. The topological analysis of the charge density, $\rho(r)$, according to the Bader quantum theory of atoms in molecules and crystals,[31,32] as implemented in the TOPOND code,[33] was exploited to explore the bonding framework and analyze the incoming interactions along the reaction path. A fully automated eigenvector-following numerical procedure was used to find the critical points (CP) of the charge density that were classified according to the sign of the 3 nonzero eigenvalues of the Hessian matrix as (3,−3), (3,−1), (3,+1), and (3,+3). If (3,−3), which is the maxima of the charge density, identifies the position of the nuclei, the (3,−1) CPs correspond to the maxima in two directions and the minima along the axes between two atoms, and are called bond critical points (BCP). The (3,+1) and (3,+3) CPs represent local minima and indicate the zone in which the charge density is depleted. The BCP of magnesium atoms along the migration path has been characterized by means of a series of topological indicators to provide a provisional classification of the type of interactions. Finally, some atomic properties as energy, volume, and charge, obtained by integrating $\rho(r)$ within each atomic basin, were calculated for some of the atoms involved in the Mg migration. In all cases, the most stringent tolerances were used for the integration grids and to determine the atomic boundary.[33]

2.2. DFT Modeling. DFT calculations were performed using different well-known codes such as Vienna Ab initio Simulation Package (VASP),[34] Quantum Espresso,[35,36] and CRYSTAL.[37] The first two packages employ plane-wave basis sets, while the last one employs a local atom-centered Gaussian basis set.

A full relaxation (cell shape/volume and atom positions) of the initial crystal structure was performed using the projector-augmented wave (PAW) approach with the Perdew−Burke−Ernzerhof (PBE)[38] exchange−correlation functional, as implemented in VASP and Quantum Espresso. D2 dispersive corrections[39] have been used to better account for van der Waals interactions.

In VASP, the recommended PAW pseudopotentials were used for each chemical element. The convergence of the total energy value, unit cell vector length, and orientation was achieved with respect to the plane-wave kinetic energy cutoff value (800 eV) and density of the reciprocal space sampling within the Monkhorst−Pack scheme.

Quantum Espresso geometry optimizations were performed with the nonlocal vdW-DF2 method[40] with the efficiency set of standard solid-state pseudopotentials (SSSP) from Materials cloud,[41−43] imposing an energy cutoff of 60 Ry (~816 eV).

All calculations were run twice. In the first run, the lattice parameters were taken from the Rietveld refinement and kept fixed, while the atomic positions were optimized. In the second run, the lattice parameters were also optimized.

In CRYSTAL, basis sets from the public CRYSTAL database have been used: a 6-311G(d) on N, a modified Pople 6-21G* on B, 8-511G(d) on Mg, and 3-11G on H. An 8 × 8 × 8 Monkhorst−Pack grid has been used to sample the reciprocal space.

The most probable pathway for ionic mobility was modeled as a transition of Mg^{2+} from one vacant equilibrium position to another (which corresponds to an ion-vacancy exchange) and evaluated by means of the climbing image (CI) NEB as implemented in Quantum Espresso. Four CI-NEB steps were performed, with 10, 14, 26, and 26 intermediate images,

https://doi.org/10.1021/acs.jpcc.2c04934
J. Phys. Chem. C 2022, 126, 15118−15127

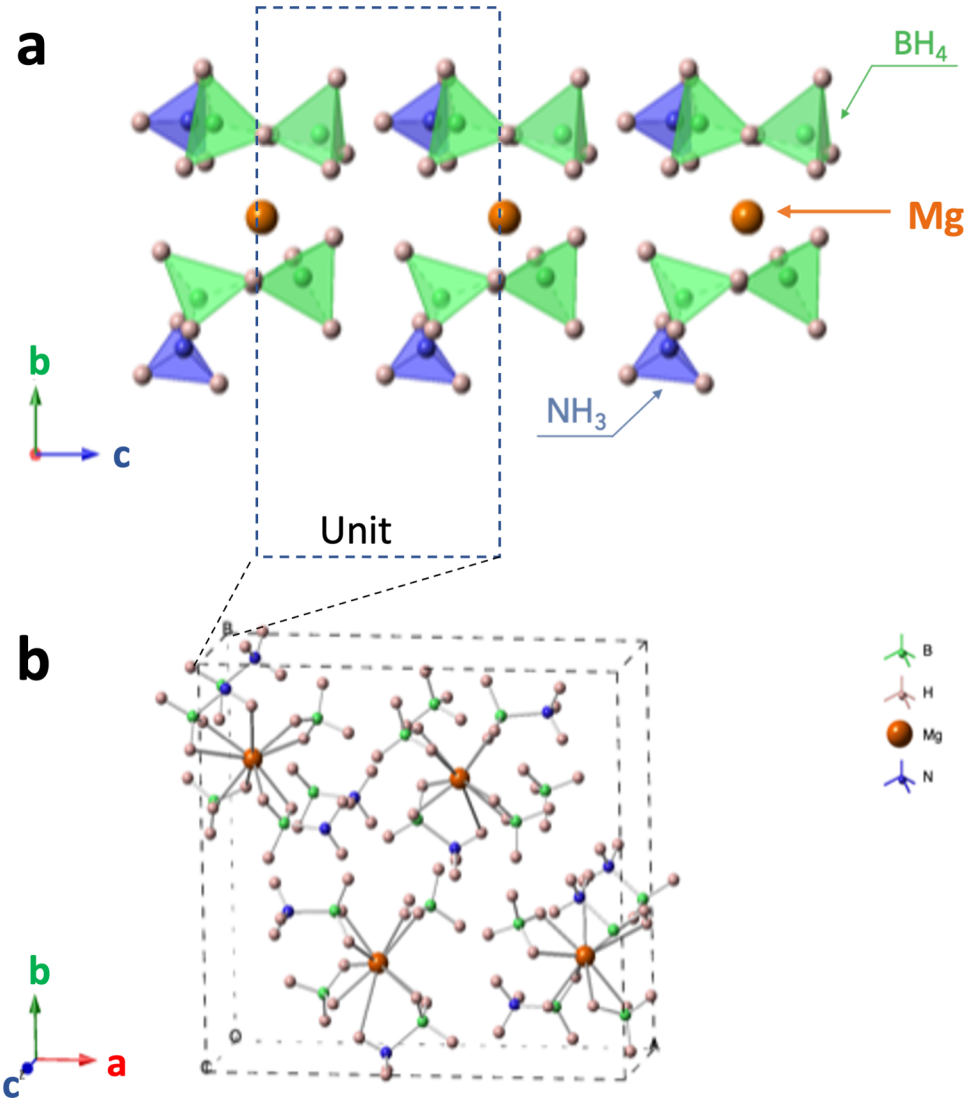

Figure 1. Crystal structure of magnesium borohydride ammonia borane $Mg(BH_4)_2(NH_3BH_3)_2$ (Mg atoms are in orange, B atoms in green, N atoms in blue, and H atoms in pink).

respectively. Only the last step was performed as the full CI-NEB methodology.

The defect formation energy was calculated following an approach proposed by Van de Walle et al.,[44] where the energy of a single defect or impurity is obtained from the difference between the total energy derived from a supercell calculation with one defect and the total energy from an equivalent supercell with no defect, plus some correction terms. These terms can be, for example, the chemical potential of the created defect and represent the energy of the reservoirs, with which the atoms are being exchanged. In this work, a 1 × 1 × 2 supercell and the VASP code were used for defect calculations.

For phonon calculations in the harmonic approximation, the Phonopy package was used.[45] The dynamical matrix was obtained by the direct method (supercell method). The unit cell was first further relaxed with VASP until the residual forces on each atom were less than 5 meV $Å^{-1}$. Afterward, 162 atomic displacements were generated according to the crystal symmetry in 1 × 1 × 2 supercells and atomic forces were computed using VASP. To reduce numerical noise, central differences were applied to obtain the force constants matrix. The Phonopy package was then applied to diagonalize the dynamical matrix and obtain phonon frequencies. The phonon density of states (DOS) was calculated by integrating over the first Brillouin zone with an equispaced q-point mesh of adequate size. For computing infrared (IR) and Raman spectra, phonon modes close to the Γ point were considered as they interact with the visible and infrared radiation used in experiments. Hence, IR and Raman spectra are essentially a phonon DOS for **q**-vectors close to the Γ point with intensities weighted by the spectroscopic activity of the phonon modes. The spectroscopic activities were then calculated following the approach detailed in refs 46, 47. The absolute infrared activities I_{IR} are given by the square of the change in the macroscopic polarization $\boldsymbol{P}$, i.e., the dipole moment for unit volume, with respect to displacement along the normal-mode coordinates. The change in the polarization is obtained from the Born effective-charge tensors $\mathbf{Z}^*$ for each atom i defined as

$$Z^*_{\alpha\beta}(\mathrm{i}) = \frac{\Omega}{e}\frac{\partial P_\alpha}{\partial r_\beta(\mathrm{i})} \tag{3}$$

where α and β are Cartesian coordinates (x, y, z), Ω is the unit cell volume, e is the electronic charge, and $\boldsymbol{r}$ is the displacement

https://doi.org/10.1021/acs.jpcc.2c04934
J. Phys. Chem. C 2022, 126, 15118−15127

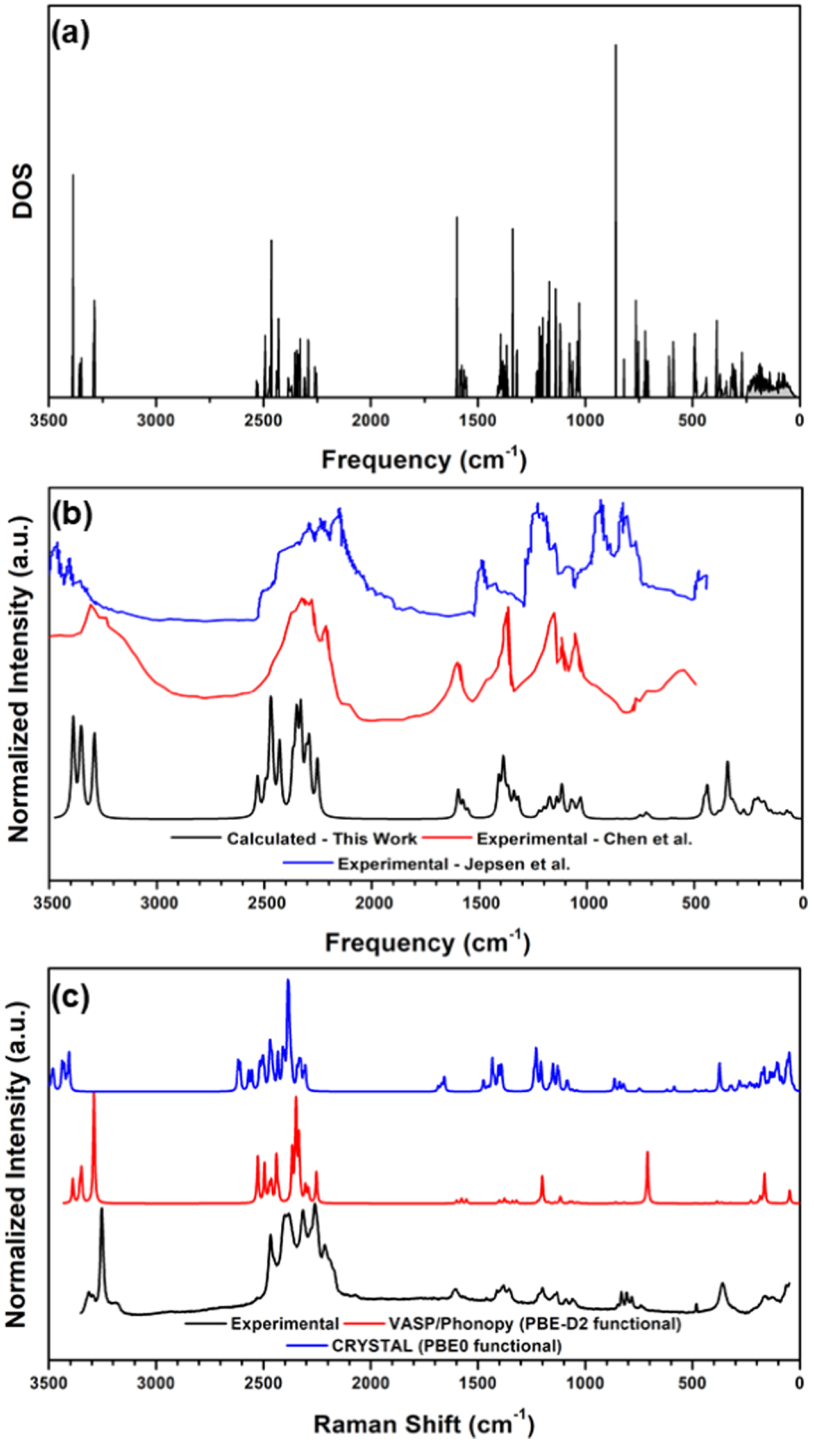

Figure 2. (a) Total phonon DOS for $Mg(BH_4)_2(NH_3BH_3)_2$ calculated with VASP/Phonopy and the PBE-D2 functional and (b) calculated IR spectra using VASP/phonopy and the PBE-D2 functional (corresponding optimized lattice parameters are shown in Table 1). The experimental IR spectra are from Chen et al.[30] and Jepsen et al.[29] (c) calculated Raman spectra using VASP/phonopy (PBE-D2 functional; red line) and CRYSTAL (PBE0 functional; blue line). The corresponding optimized lattice parameters are shown in Table 1. A constant Gaussian broadening of 8 cm^{-1} was applied to the calculated spectra. The experimental Raman spectra, black line, are from this work. Further details are given in the text.

of the atom *i*. These **Z*** tensors were computed using density functional perturbation theory (DFPT) as implemented in VASP (LESPILON = True) and in CRYSTAL. Similarly, the Raman activities I_{Raman} are given by the change in the polarizability tensor $\boldsymbol{\alpha}$ along the normal-mode directions, which can be obtained from the macroscopic dielectric constant. The latter can be obtained using DFPT as implemented in VASP (LESPILON = True) and in CRYSTAL with atoms properly displaced along the mode eigenvectors and using a central difference scheme to derive the variation.[46] A proper averaging to account for measurement geometrical factors must also be applied as described in ref 47. Though in principle, the broadening of IR and Raman spectral lines can be derived from phonon lifetimes, these calculations were

https://doi.org/10.1021/acs.jpcc.2c04934
J. Phys. Chem. C 2022, 126, 15118−15127

beyond the scope of this work and the computational effort required is still daunting for the complex unit cell as that of the present system. Hence, a Lorentzian function with a full width at half maximum of 16 cm^{-1} was applied to approximately reproduce peak broadening in both IR and Raman calculated spectra.

2.3. Experimental Section. $Mg(BH_4)_2(NH_3BH_3)_2$ was prepared via a mechanical milling method. In an Ar-filled glovebox, $Mg(BH_4)_2$ (>95%, Sigma-Aldrich) and NH_3BH_3 (>97%, Sigma-Aldrich) were mixed thoroughly in a molar ratio of 1:2 for 15 min in an agate mortar. This mixture was then transferred into a 45 mL Cr-hardened stainless-steel vessel with 20 SUJ2 balls (diameter: 7 mm) and mixed using a planetary ball mill (P-7, Fritsch) at 260 rpm for 4 h in an Ar-filled environment. The vibrational modes of a $[BH_4]^-$ anion and a NH_3BH_3 molecule in prepared $Mg(BH_4)_2(NH_3BH_3)_2$ were characterized by Raman spectroscopy with a 532 nm laser (DXR, Thermo Scientific).

2.4. Structure Visualization. We used the VESTA visualization package[48] to prepare some of the figures.

3. RESULTS AND DISCUSSION

3.1. DFT Analysis. As a first step, we relaxed the initial (experimental) crystal structure of $Mg(BH_4)_2(NH_3BH_3)_2$ using different packages and functionals. The optimized crystal structure is shown in Figure 1, while the calculated lattice parameters after relaxation are compared with experimental results in Table 1. The experimental results lie in between calculated results obtained with the PBE and PBE-D2 functional. The weak interactions in the plane-wave approaches are usually overestimated (VASP PBE-D2), resulting in a smaller cell volume. Using the nonlocal vdW-DF2 method (QE), which is also less sensitive to the choice of pseudopotentials, the shrinking of the cell is less pronounced.

The thermodynamic stability of the compound was also estimated by computing its formation energy using the VASP code, i.e., the energy change related to the following reaction

$$Mg(hcp) + 4\,B(rhombohedral) + 2\,N_2(gas) + 18\,H_2(gas) \rightarrow Mg(BH_4)_2(NH_3BH_3)_2$$

It is worth noting that it is still under discussion which is the stable allotrope of elemental boron at room temperature, though the difference in energy between the allotropes is of the order of 0.1 kJ mol^{-1} of at.[49] In our calculations, at 0 K, we have used the α rhombohedral structure for pure boron. According to this choice, the computed enthalpy of formation is −25.1 kJ mol^{-1} with the PBE functional and −25.2 kJ mol^{-1} with the PBE-D2 including Grimme's corrections.

From the 108 atoms in the relatively large unit cell, a total of 324 phonon bands for each q-point in the Brillouin zone are obtained, and the resulting phonon dispersion curves and DOS are significantly complex. Figures 2a and S1 (Supporting Material) show the calculated total and partial phonon density of states (DOS) obtained using VASP and Phonopy. The phonon frequencies span a range of approximately 3500 cm^{-1}, with the low-frequency part of the phonon DOS relatively continuous, whereas at higher frequencies, several "phonon band gaps" appear. In particular, there are two groups of peaks for frequencies at around 2300−2500 and 3300−3400 cm^{-1}, which appear well separated from the lowest part of the spectrum. The partial phonon DOS shows that the heavier Mg atoms are involved in phonon modes at low frequencies, while lighter B, N, and H atoms dominate the high-frequency part of the spectrum. In particular, the phonon modes at around 2300−2500 cm^{-1} are only due to the vibration of B−H bonds and phonon modes at around 3300−3400 cm^{-1} are only due to the vibration of N−H bonds.[50] In the middle part of the spectrum (500−1500 cm^{-1}), vibrational modes including B, N, and H atoms are dominant.

The IR and Raman activities for each phonon mode at the Γ point have been calculated as described in detail in the Methods Section. The resulting intensities are reported in Tables S2 and S3 in Supporting Information. The 321 optical modes deriving from the crystal structure reduce to Γ = 81 A + 80 B1 + 80 B2 + 80 B3. The calculated IR and Raman spectra are shown in Figure 2. We already remarked that the peak broadening in these spectra was obtained by applying a Lorentzian function with a constant full width at half maximum of 16 cm^{-1}. The most prominent calculated IR modes are the B1 mode at 2470 cm^{-1}, the B2 mode at 2429 cm^{-1}, the B3 mode at 2348 cm^{-1}, and the B2 mode at 2331 cm^{-1}, which lead to the wide range of IR peaks at 2200−2600 cm^{-1}. Other prominent IR modes appear at 1388 cm^{-1} and in the high-frequency range of 3200−3500 cm^{-1}. The A modes are IR inactive. The calculated IR spectra are shown in Figure 2b, together with the experimental spectra obtained by Chen et al.[30] and by Jepsen et al.[29] A quite good agreement can be observed between the calculated and experimental IR peaks, though some experimental peaks appear slightly shifted compared to the calculated ones, and the broadening of the first is higher. The shift is due to the well-known overestimation of vibrational frequencies when using the PBE and PBE-related functionals, and it also occurs in the Raman spectra.

The most prominent calculated Raman modes are at 3291, 2349, and 2335 cm^{-1} (all A modes). An important B1 mode is also calculated at 710 cm^{-1}. Most of the highest Raman peaks are, in fact, A and B1 modes. The calculated Raman spectra obtained both with VASP and CRYSTAL codes are compared with the experimental results in Figure 2c. An excellent agreement can be noticed in the middle-/high-frequency part of the spectra, while some disagreement occurs at low frequencies. In this latter region, results with the hybrid functional and CRYSTAL appear to be better than VASPs with the PBE-D2 functional. The origin of these discrepancies can be in experimental issues such as instrumental broadening or fluorescence background. Part of the disagreement could also be related to the applied Lorentzian broadening compared to a full calculation including phonon lifetimes. However, the overall agreement is very satisfactory and confirms that the present DFT calculations describe well the properties of this system.

3.2. Topological Analysis. The first screening of possible pathways for Mg ion migration was conducted by analyzing the calculated charge density, as shown in Figure 3a. It is evident that there are regions within the cell where the density of charge is almost negligible, as revealed by the presence of numerous critical points of the charge density (CPs) (3,+1) and (3,+3) CPs, represented with gray and black spots in Figure 3a. The mobility of the large Mg^{2+} ions along these corridors, where the electronic charge is minimal, is expected to be relatively high since it is not hindered by Coulombic repulsions. The red arrows in Figure 3b show a possible migration path along the c-axis in a channel surrounded by NH_3 tetrahedra, hypothesized on the basis of topological

https://doi.org/10.1021/acs.jpcc.2c04934
J. Phys. Chem. C 2022, 126, 15118−15127

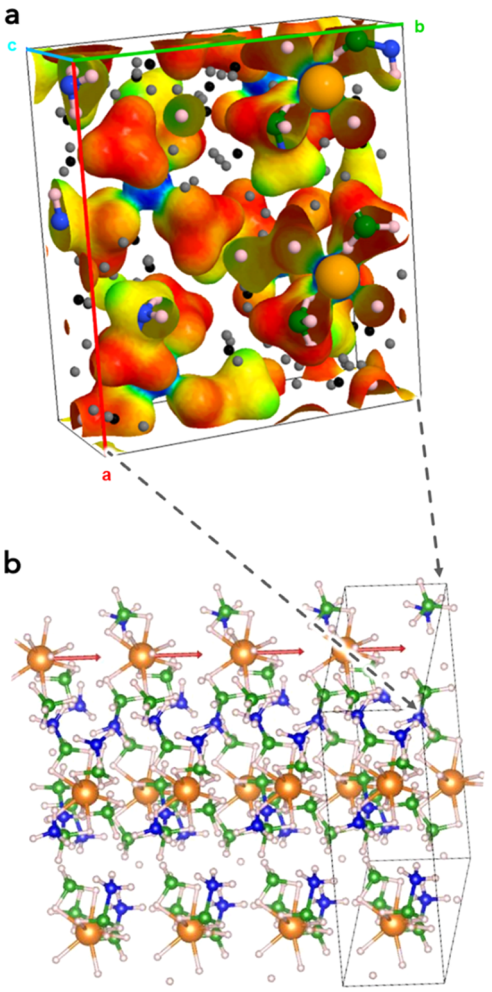

Figure 3. (a) Charge density of $Mg(BH_4)_2(NH_3BH_3)_2$ calculated with the CRYSTAL code. Mg atoms are in orange, B atoms in green, N atoms in blue, and H atoms in pink. The gray and blank spots represent the position of (3,+1) and (3,+3) critical points of the charge density, respectively. (b) Migration path of Mg atoms within the QE optimized cell. Four unit cells are stacked on the *c*-axis, and the red arrow displays the Mg migration path along the *c*-axis selected for QE-NEB calculations. Mg atoms are in orange, B atoms in green, N atoms in blue, and H atoms in pink.

indicators, from which the CI-NEB analysis (see the next subsection) started for the identification of the minimum energy path.

To analyze the bonding framework along this path, the values of three topological descriptors, namely, the Laplacian of the charge density, $\nabla^2\rho(\boldsymbol{r})$, the ratio between the virial density, $V(\boldsymbol{r})$, and kinetic energy density, $G(\boldsymbol{r})$, $|V(\boldsymbol{r})|/G(\boldsymbol{r})$, and the ratio between the total energy density, $H(\boldsymbol{r}) = V(\boldsymbol{r}) + G(\boldsymbol{r})$, and the charge density, $H(\boldsymbol{r})/\rho(\boldsymbol{r})$, referred also as bond order, were evaluated in $\boldsymbol{r} = \boldsymbol{r}_{BCP}$ and compared. According to our results, reported in Table 2, each Mg atom interacts with its first coordination sphere of hydrogens through weak van der Waals forces, as already documented in other theoretical studies on Mg compounds.[51] In fact, in all of the Mg−H BCPs (bond CPs), the density is extremely low, the Laplacian is positive, and the two energetic components, potential and kinetics, are perfectly balanced, so the interaction is neither ionic nor covalent. Along the way, as Mg migrates, some Mg−H bonds weaken while others form. Interestingly enough, in the two transition states, a boron atom enters the coordination sphere of Mg, as revealed by the presence of a BCP along the Mg−B direction.

Table 2. Values of the Topological Descriptors Calculated in the r_{BCP} of the Migrating Mg Atom[a]

X	ρ (r)	$\nabla^2\rho$ (r)	V (G)	H (ρ(r))
Initial Geometry				
H-*i*	0.024	0.076	1.015	−0.012
H_2	0.028	0.086	1.056	−0.046
H_3	0.024	0.076	1.004	−0.003
Transition State 1 (Conf. 6)				
H-i	0.012	0.030	0.990	0.006
B-f	0.031	0.091	1.105	−0.086
H_2	0.031	0.091	1.105	−0.084
H_3	0.015	0.044	0.982	0.013
H_4	0.019	0.062	0.986	0.011
Relative Minimum (Conf. 12)				
H_4	0.024	0.081	0.989	0.009
H-f	0.028	0.080	1.081	−0.064
Transition State 2 (Conf. 18)				
B-f	0.026	0.076	1.065	−0.050
H-f	0.025	0.075	1.052	−0.040
H_3	0.015	0.043	1.000	0.000
H_4	0.019	0.053	1.024	−0.018

[a]Only the first coordination sphere is reported. The configurations are labeled according to Figure 5. The charge density, ρ (r), and its Laplacian are in Au.

To further characterize the perturbation induced by the migration, the hydrogen and boron atoms closest to magnesium in the initial (H-i, B-i) and final configuration (H-f, B-f) were selected, and the differences in energy, charge, and volume with respect to their values in the initial geometry were calculated and are reported in Figure 4 (see below for the definition of the migration path and sampling images). Incidentally, it can be noted that the B-i does not appear in Table 2 because no BPC was detected between these two atoms. During its migration, Mg preserves the charge while both the volume and the energy density are changing and, in the transition states, the increase of the atomic volume is associated with higher chemical potential. No significant charge transfers are observed in the atoms involved in the migration process, as shown in Figure 4a, where it is seen that all of the differences are within a rather narrow range. A quick comment can be made on the slight loss of charge by the hydrogen atoms, quantified by the positive values shown in Figure 4a (square symbols) due to the step away of the magnesium. Finally, based on the atomic energies calculated in each configuration, it is possible to estimate the contribution of each atom to the total energy. Although only a few atoms involved have been analyzed, it can already be noted that the relevant part of the activation barrier is due to the Mg and boron atoms (Figure 4b, circles and triangles).

3.3. DFT Climbing Image Nudged Elastic Band (CI-NEB). As described in the previous subsection, CI-NEB calculations were performed along the most probable migration path of Mg atoms (Figure 3) to determine the migration energy. Considering the difficulties and relative sensibility of these calculations, we decided to investigate the process with three different approaches, QE, VASP, and CRYSTAL.

https://doi.org/10.1021/acs.jpcc.2c04934
J. Phys. Chem. C 2022, 126, 15118−15127

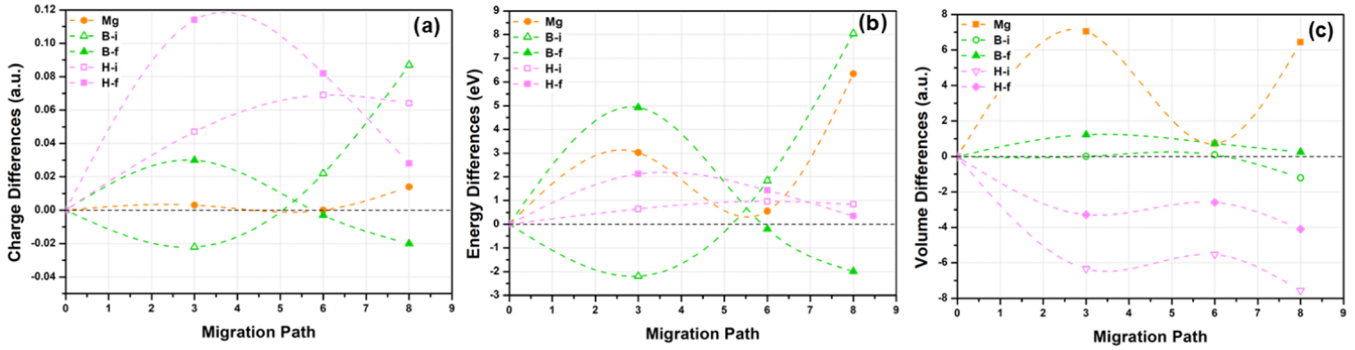

Figure 4. (a) Bader charges, (b) atomic energies in eV, and (c) volumes in A (bottom) are reported as a difference with respect to their values in the initial configuration for Mg (orange circle) B-i and B-f (empty and filled green triangles, respectively) H-i and H-f (empty and filled pink squares, respectively). Image (or configuration) 0 is the initial relaxed structure, image x = 3 is the first maximum, image x = 6 is the local minimum, and image x = 8 is the second maximum (cfr. Figure 5).

The DFT total energies of the images along the pathway calculated using the CI-NEB method and Quantum espresso are shown in Figure 5, along with the intermediate structures as found during CI-NEB calculations, namely, sampling images (geometries) along the transition process. As it can be seen, there are three maxima in energy along the path. Taking as reference the energy of the equivalent structures at the beginning and end of Mg movement (configurations or images 1 and 26 as an inset in Figure 5), corresponding to the relaxed initial structure, the first (local) maximum is observed at 0.5044 eV (image 6) followed by a deep local minimum with an energy of just 0.0598 eV (image 12). The CI-NEB profile along the path shows again an increase in energy up to another local maximum, but in this case, the highest point is at 0.6684 eV (image 19). The latter is then the migration energy along this pathway estimated by the CI-NEB method and Quantum Espresso.

To further verify the obtained energy profile, calculations have been carried out on selected images along the pathway with both VASP and CRYSTAL. The results are also shown in Figure 5. Both profiles calculated with CRYSTAL and VASP confirm the energy values obtained with Quantum Espresso. VASP results using both PBE and PBE-D2 functionals (E_m = 0.682 eV for PBE, E_m = 0.550 eV for PBE-D2) are very close to the migration energy obtained with Quantum Espresso. The three local maxima in the energy profile found with VASP correspond to those obtained with Quantum Espresso. CRYSTAL results are slightly higher, E_m = 0.885 eV for PBE-D2 and 0.989 for PBE0-D3. Considering the entirely different approach implemented by the codes and the different roles of computational thresholds, these results are in substantial agreement.

3.4. Defect Formation and Activation Energy. Finally, the energy for defect formation has been estimated using the VASP code as detailed in the Methods Section. It must be remarked that such calculations are not trivial, as several mechanisms and defect types can occur at the same time. Here, we assumed that the dominant defect type is a Frenkel pair, i.e., the formation of an interstitial Mg^{2+} defect together with a vacancy Va^{2-}. The formation mechanism is then the displacement of a Mg^{2+} ion from its initial position to an interstitial site, leaving behind a vacancy. Several interstitial positions are possible, and the one with minimum energy provides the formation energy for the Frenkel pair. The validity of this assumption can be evaluated a posteriori by comparison with experimental results of the activation energy for ion

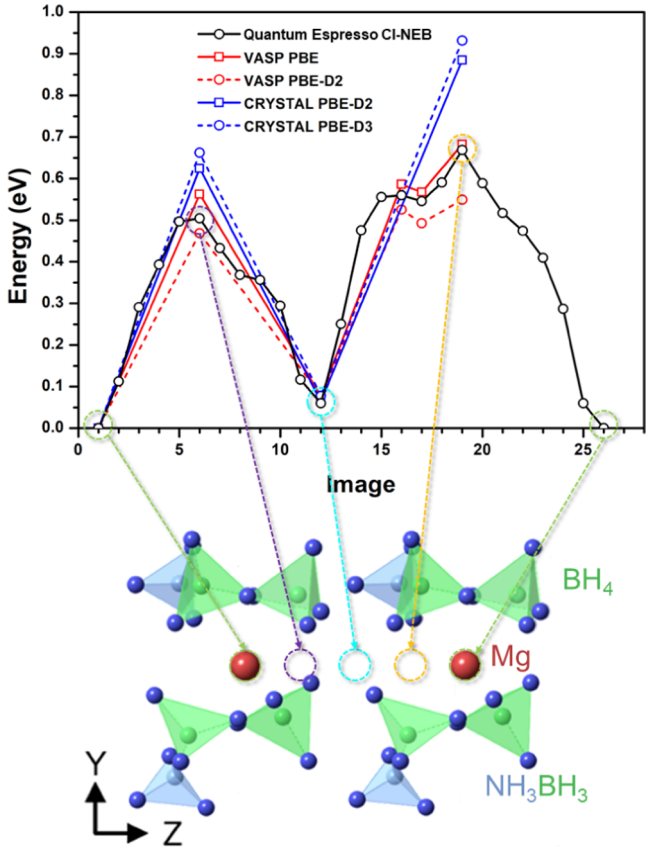

Figure 5. CI-NEB total energy profiles for the Mg^{2+} pathway as calculated with Quantum Espresso, VASP, and CRYSTAL. The crystal structures show the position of the Mg ion in the most significant points of the energy profile. Image (or configuration) 0 is the initial relaxed structure, image 6 is the first maximum, image 12 is the local minimum, and image 19 is the second maximum.

migration obtained from measurements of conductivity at different temperatures. It has already been successfully applied in other systems.[52]

The resulting calculated energy for the formation of the Frenkel pair (E_f) is equal to 2.09 eV using the PBE-D2 functional. By inserting this result into eq 1, we obtain a total value for the activation energy of Mg^{2+} ion migration of E_A = 1.60 eV (using the PBE-D2 value obtained with VASP for E_m) or E_A = 1.71 eV (using the value obtained with Quantum

https://doi.org/10.1021/acs.jpcc.2c04934
J. Phys. Chem. C 2022, 126, 15118−15127

Espresso for E_m). Both results are in satisfactory agreement with the experimental value of 1.47 ± 0.03 eV calculated by linear fitting of $\ln(\sigma T)$ and $1000/T$ (95% of confidence) of the literature data taken from ref 23.

4. CONCLUSIONS

In summary, magnesium borohydride ammonia borane, $Mg(BH_4)_2(NH_3BH_3)_2$, was theoretically investigated using different density functional theory (DFT) approaches and software. Considering room temperature, the calculated activation energy for Mg migrations shows a relatively high conductivity with respect to the original $Mg(BH_4)_4$, in agreement with experimental findings. The crystal structure was optimized, and the calculated values of the lattice parameters bracket the experimental ones depending on the different calculation setups, the most significant differences arising from different exchange−correlation functionals (some including weak van der Waals interactions). The topological analysis based on the calculated charge density suggests one of the possible paths for Mg ion migration, which was further investigated with CI-NEB calculations. Furthermore, it shows that weak van der Waals forces are relevant in the Mg−Hs interactions and are preserved along the whole Mg path during ion migration. The two transition states found in this analysis also suggest repulsive interactions between the Mg and B atoms.

The calculated vibrational properties in the harmonic approximation show a complex phonon DOS where the heavier Mg atoms dominate, as expected, the low-frequency part of the phonon DOS, while H, B, and N atoms prevail at high frequencies. Several "phonon band gaps" were also found, and high-frequency peaks are well separated from the lower part of the spectrum. The calculated IR and Raman spectra compare well with the experimental data.

Calculated CI-NEB results show a complex energy landscape with two local maximum in the energy and a deep local minimum in between along the selected migration path for Mg^{2+} ions. These findings are confirmed by all computer codes used. The calculated migration energies (including weak van der Waals interactions) are in the range of 0.550−0.668 eV using plane-wave codes. Including the calculated defect (Frenkel pairs) formation energy of 1.05 eV (per single defect), a value of the activation energy for migration in the range of 1.60−1.71 eV is found. This compares relatively well with the experimental estimation of 1.47 ± 0.03 eV within the approximations adopted, suggesting that the above approach is correct and the dominant type of defect is, in fact, Frenkel pair. As a future study, we plan to compare and complement our findings with other mechanisms proposed in the recent literature.[54,55]

■ ASSOCIATED CONTENT

Supporting Information

The Supporting Information is available free of charge at https://pubs.acs.org/doi/10.1021/acs.jpcc.2c04934.

Details on computed vibrational Raman frequencies (PDF)

■ AUTHOR INFORMATION

Corresponding Authors

Mauro Palumbo − *Department of Chemistry and NIS-INSTM, University of Turin, I-10125 Torino, Italy*; Email: mauro.palumbo@unito.it

Lorenzo Maschio − *Department of Chemistry and NIS-INSTM, University of Turin, I-10125 Torino, Italy*; orcid.org/0000-0002-4657-9439; Email: Lorenzo.maschio@unito.it

Authors

Kazuaki Kisu − *Institute for Materials Research (IMR), Tohoku University, 980-8577 Sendai, Japan*

Valerio Gulino − *Materials Chemistry and Catalysis, Debye Institute for Nanomaterials Science, Utrecht University, 3584 CG Utrecht, The Netherlands*; orcid.org/0000-0002-5808-7802

Carlo Nervi − *Department of Chemistry and NIS-INSTM, University of Turin, I-10125 Torino, Italy*; orcid.org/0000-0002-3712-7369

Silvia Casassa − *Department of Chemistry and NIS-INSTM, University of Turin, I-10125 Torino, Italy*; orcid.org/0000-0003-0217-4920

Shin-ichi Orimo − *Institute for Materials Research (IMR), Tohoku University, 980-8577 Sendai, Japan; Advanced Institute for Materials Research (WPI-AIMR), Tohoku University, 980-8577 Sendai, Japan*

Marcello Baricco − *Department of Chemistry and NIS-INSTM, University of Turin, I-10125 Torino, Italy*; orcid.org/0000-0002-2856-9894

Complete contact information is available at: https://pubs.acs.org/10.1021/acs.jpcc.2c04934

Notes

The authors declare no competing financial interest.

The authors declare that the data supporting the findings of this study are available within the paper. Raw data can be provided upon reasonable request.

■ ACKNOWLEDGMENTS

M.P. would like to thank the "Centro di Competenza sul Calcolo Scientifico" for the computing time on the OCCAM supercomputer.[53] This work was partially supported by JSPS KAKENHI of Young Scientists (No. 19K15305) and Grant-in-Aid for Scientific Research on Innovative Areas "Hydrogenomics" (No. JP18H05513).

■ REFERENCES

(1) Tian, Y.; Zeng, G.; Rutt, A.; et al. Promises and Challenges of Next-Generation "beyond Li-ion" Batteries for Electric Vehicles and Grid Decarbonization. *Chem. Rev.* **2020**, *121*, 1623−1669.

(2) Kisu, K.; Kim, S.; Shinohara, T.; Zhao, K.; Züttel, A.; Orimo, S. Monocarborane Cluster as a Stable Fluorine-free Calcium Battery Electrolyte. *Sci. Rep.* **2021**, *11*, No. 7563.

(3) Aurbach, D.; Lu, Z.; Schechter, A.; Gofer, Y.; Gizbar, H.; Turgeman, R.; Cohen, Y.; Moshkovich, M.; Levi, E. Prototype Systems for Rechargeable Magnesium Batteries. *Nature* **2000**, *407*, 724−727.

(4) Mohtadi, R.; Orimo, S. I. The Renaissance of Hydrides as Energy Materials. *Nat. Rev. Mat.* **2017**, *2*, No. 16091.

(5) Skov, L. N.; Grinderslev, J. B.; Rosenkranz, A.; Lee, Y.-S.; Jensen, T. R. Towards Solid State Magnesium Batteries: Ligand-Assisted Superionic Conductivity. *Batteries Supercaps* **2022**, No. e202200163.

(6) Kristensen, L. G.; Amdisen, M. B.; Skov, L. N.; Jensen, T. R. Fast Magnesium Ion Conducting Isopropylamine Magnesium Borohydride Enhanced by Hydrophobic Interactions. *Phs. Chem. Chem. Phys.* **2022**, *24*, 18185−18197.
(7) Yan, Y.; Grinderslev, J. B.; Jorgensen, M.; Skov, L. N.; Skibsted, J.; Jensen, T. R. Ammine Magnesium Borohydride Nanocomposites for All-Solid-State Magnesium Batteries. *ACS Appl. Energy Mater.* **2020**, *3*, 9264−9270.
(8) Yan, Y.; Grinderslev, J. B.; Burankova, T.; Wei, S.; Embs, J. P.; Skibsted, J.; Jensen, T. R. Fast Room-Temperature Mg2+Conductivity in Mg(BH4)2·1.6NH3- Al2O3Nanocomposites. *J. Phys. Chem. Lett.* **2022**, *13*, 2211−2216.
(9) Grinderslev, J. B.; Amdisen, M. B.; Skov, L. N.; Møller, K. T.; Kristensen, L. G.; Polanski, M.; here, M.; Jensen, T. R. New Perspectives of Functional Metal Borohydrides. *J. Alloys Compd.* **2022**, *896*, No. 163014.
(10) Cuevas, F.; Amdisen, M. B.; Baricco, M.; et al. Metallic and Complex Hydride-based Electrochemical Storage of Energy. *Prog. Energy* **2022**, *4*, No. 032001.
(11) Unemoto, A.; Matsuo, M.; Orimo, S. I. Complex Hydrides for Electrochemical Energy Storage. *Adv. Funct. Mater.* **2014**, *24*, 2267−2279.
(12) Muldoon, J.; Bucur, C. B.; Gregory, T. Quest for Nonaqueous Multivalent Secondary Batteries: Magnesium and Beyond. *Chem. Rev.* **2014**, *114*, 11683−11720.
(13) Ha, S. Y.; Lee, Y.-W.; Woo, S. W.; Koo, B.; kim, J.-S.; Cho, J.; lee, K. T.; Choi, N.-S. Magnesium(II) bis(trifluoromethane sulfonyl) Imide-Based Electrolytes with Wide Electrochemical Windows for Rechargeable Magnesium Batteries. *ACS Appl. Mater. Interfaces* **2014**, *6*, 4063−4073.
(14) Tutusaus, O.; Mohtadi, R.; Arthur, T. S.; MizAuno, F.; Nelson, E. G.; Sevryugina, Y. V. An Efficient Halogen-Free Electrolyte for Use in Rechargeable Magnesium Batteries. *Angew. Chem., Int. Ed.* **2015**, *54*, 7900−7904.
(15) Kato, Y.; Hori, S.; Saito, T.; Suzuki, K.; Hirayama, M.; Mitsui, A.; Yonemura, M.; Iba, H.; Kanno, R. High-Power all-Solid-State Batteries using Sulfide Superionic Conductors. *Nat. Energy* **2016**, *1*, No. 16030.
(16) Kim, S.; Oguchi, H.; Toyama, N.; et al. A Complex Hydride Lithium Superionic Conductor for High-Energy-Density all-Solid-State Lithium Metal Batteries. *Nat. Commun.* **2019**, *10*, No. 1081.
(17) Jaschin, P. W.; Gao, Y.; Li, Y.; Bo, S. H. A Materials Perspective on Magnesium-Ion-Based Solid-State Electrolytes. *J. Mater. Chem. A* **2020**, *8*, 2875−2897.
(18) Higashi, S.; Miwa, K.; Aoki, M.; Takechi, K. A Novel Inorganic Solid State ion Conductor for Rechargeable Mg Batteries. *Chem. Commun.* **2014**, *50*, 1320−1322.
(19) Burankova, T.; Roedern, E.; Maniadaki, A. E.; Hagemann, H.; Rentsch, D.; Lodziana, Z.; Battaglia, C.; Remhof, A.; Embs, J. P. Dynamics of the Coordination Complexes in a Solid-State Mg Electrolyte. *J. Phys. Chem. Lett.* **2018**, *9*, 6450−6455.
(20) Roedern, E.; Kühnel, R.-S.; Remhof, A.; Battaglia, C. Magnesium Ethylenediamine Borohydride as Solid-State Electrolyte for Magnesium Batteries. *Sci. Rep.* **2017**, *7*, No. 46189.
(21) Ikeshoji, T.; Tsuchida, E.; Takagi, S.; Matsuo, M.; Orimo, S. I. Magnesium Ion Dynamics in Mg(BH4)2(1-x)X2x (X = Cl or AlH4) from First-Principles Molecular Dynamics Simulations. *RSC Adv.* **2014**, *4*, 1366−1370.
(22) Matsuo, M.; Oguchi, H.; Sato, T.; Takamura, H.; Tsuchida, E.; Ikeshoji, B.; Orimo, S.-I. Sodium and Magnesium Ionic Conduction in Complex Hydrides. *J. Alloys Compd.* **2013**, *580*, S98−S101.
(23) Kisu, K.; Kim, S.; Inukai, M.; Oguchi, H.; Takagi, S.; Orimo, S.-I. Magnesium Borohydride Ammonia Borane as a Magnesium Ionic Conductor. *ACS Appl. Energy Mater.* **2020**, *3*, 3174−3179.
(24) Kittel, C. *Introduction to Solid State Physics*; Wiley, 2005.
(25) Goodenough, J. B. Oxide-Ion Electrolytes. *Annu. Rev. Mater. Res.* **2003**, *33*, 91−128.
(26) Goodenough, J. B. Fast Ionic Conduction in Solids. *Proc. R. Soc. London, Ser. A* **1984**, *393*, 215−234.
(27) Urban, A.; Seo, D. H.; Ceder, G. Computational Understanding of Li-ion Batteries. *npj Comput. Mater.* **2016**, *2*, No. 16002.
(28) Baktash, A.; Reid, J. C.; Roman, T.; Searles, D. J. Diffusion of Lithium Ions in Lithium-Argyrodite Solid-State Electrolytes. *npj Comput. Mater.* **2020**, *6*, No. 162.
(29) Jepsen, L. H.; Ban, V.; Møller, K.; Lee, Y.-S.; Cho, Y.-W.; Besenbacher, F.; Filinchuk, Y.; Skibsted, J.; Jensen, T. R. Synthesis, Crystal Structure, Thermal Decomposition, and11B MAS NMR Characterization of $Mg(BH_4)_2(NH_3BH_3)_2$. *J. Phys. Chem. C* **2014**, *118*, 12141−12153.
(30) Chen, X.; Yuan, F.; Gu, Q.; Yu, X. Synthesis, Structures and Hydrogen Storage Properties of two new H-enriched Compounds: $Mg(BH_4)_2(NH_3BH_3)_2$ and $Mg(BH_4)_2{\cdot}(NH_3)_2(NH_3BH_3)$. *Dalton Trans.* **2013**, *42*, 14365−14368.
(31) Bader, R. F. W. *Atoms in Molecules-A Quantum Theory-International Series of Monographs in Chemistry*; Oxford University Press, 1990; Vol. *22*.
(32) Gatti, C. Chemical Bonding in Crystals: New Sirections. *Z. Kristallogr. - Cryst. Mater.* **2005**, *220*, 399−457.
(33) Casassa, S.; Erba, A.; Baima, J.; Orlando, R. Electron Density Analysis of Large (molecular and periodic) Systems: A Parallel Implementation. *J. Comput. Chem.* **2015**, *36*, 1940−1946.
(34) Kresse, G.; Furthmüller, J. Efficient iterative schemes for ab initiototal-energy calculations using a plane-wave basis set. *Phys. Rev. B: Condens. Matter* **1996**, *54*, 11169−11186.
(35) Giannozzi, P.; Andreussi, O.; Brumme, T.; et al. Advanced Capabilities for Materials Modelling with Quantum Espresso. *J. Phys. Condens. Matter* **2017**, *29*, No. 465901.
(36) Giannozzi, P.; Baroni, S.; Bonini, N.; et al. QUANTUM ESPRESSO: a Modular and Open-Source Software Project for Quantum Simulations of Materials. *J. Phys. Condens. Matter* **2009**, *21*, No. 395502.
(37) Dovesi, R.; Erba, A.; Orlando, R.; et al. Quantum-Mechanical Condensed Matter Simulations with CRYSTAL. *WIREs: Comput. Mol. Sci.* **2018**, *8*, No. e1360.
(38) Perdew, J. P.; Burke, K.; Wang, Y. Generalized Gradient Approximation for the Exchange-Correlation Hole of a Many-Electron System. *Phys. Rev. B* **1996**, *54*, 16533−16539.
(39) Grimme, S. Semiempirical GGA-type Density Functional Constructed with a long-range Dispersion Correction. *J. Comput. Chem.* **2006**, *27*, 1787−1799.
(40) Lee, K.; Murray, ÉD.; Kong, L.; Lundqvist, B. I.; Langreth, D. C. Higher-Accuracy van der Waals Density Functional. *Phys. Rev. B* **2010**, *82*, No. 081101.
(41) Prandini, G.; Marrazzo, A.; Castelli, I. E.; Mounet, N.; Marzari, N. Precision and Efficiency in Solid-state Pseudopotential Calculations. *npj Comp. Mater.* **2018**, *4*, No. 72.
(42) Lejaeghere, K.; Bihlmayer, G.; Björkman, T.; et al. Reproducibility in Density Functional Theory Calculations of Solids. *Science* **1979**, *351*, No. aad3000.
(43) http://materialscloud.org/sssp.
(44) Van de Walle, C. G.; Neugebauer, J. First-principles Calculations for Defects and Impurities: Applications to III-nitrides. *J. Appl. Phys.* **2004**, *95*, 3851−3879.
(45) Togo, A.; Tanaka, I. First Principles Phonon Calculations in Materials Science. *Scr. Mater.* **2015**, *108*, 1−5.
(46) Skelton, J. M.; Burton, L. A.; Jackson, A. J.; Oba, F.; Parker, S. C.; Walsh, A. Lattice Dynamics of the Tin Sulphides SnS_2, SnS and Sn_2S_3: Vibrational Spectra and Thermal Transport. *Phys. Chem. Chem. Phys.* **2017**, *19*, 12452−12465.
(47) Jackson, K.; Pederson, M. R.; Porezak, D.; Hajnal, Z.; Frauenheim, T. Density-Functional-based Predictions of Raman and IR Spectra for Small Si Clusters. *Phys. Rev. B* **1997**, *55*, 2549−2555.
(48) Momma, K.; Izumi, F. VESTA 3 for Three-Dimensional Visualization of Crystal, Volumetric and Morphology Sata. *J. Appl. Crystallogr.* **2011**, *44*, 1272−1276.
(49) White, M. A.; Cerqueira, A. B.; Whitman, C. A.; Johnson, M. B.; Ogitsu, T. Determination of Phase Stability of Elemental Boron. *Angew. Chem., Int. Ed.* **2015**, *54*, 3626−3629.

https://doi.org/10.1021/acs.jpcc.2c04934
J. Phys. Chem. C 2022, 126, 15118−15127

(50) Matsuo, M.; Remhof, A.; Martelli, P.; et al. Complex Hydrides with (BH_4)- and (NH_2)- Anions as new Lithium Fast-Ion Conductors. *J. Am. Chem. Soc.* **2009**, *131*, 16389−16391.
(51) Albanese, E.; Civalleri, B.; Casassa, S.; Baricco, M. Investigation on the Decomposition Enthalpy of Novel Mixed $Mg(1-x)Znx(BH_4)_2$ Borohydrides by means of Periodic DFT Calculations. *J. Phys. Chem. C* **2014**, *118*, 23468−23475.
(52) Gulino, V.; Wolczyk, A.; Golov, A. A.; Eremin, R. A.; Palumbo, M.; Nervi, C.; Blatov, V. A.; proserpiuo, D. M.; Baricco, M. Combined DFT and Geometrical-Topological Analysis of Li-ion Conductivity in Complex Hydrides. *Inorg. Chem. Front.* **2020**, *7*, 3115−3125.
(53) Aldinucci, M.; Bagnasco, S.; Lusso, S.; Pasteris, P.; Rabellino, S.; Vallero, S. OCCAM: a Flexible, Multi-Purpose and Extendable HPC Cluster. *J. Phys.: Conf. Ser.* **2017**, *898*, No. 082039.
(54) Yan, Y.; Dononelli, W.; Jørgensen, M.; Grinderslev, J. B.; Lee, Y. S.; Cho, Y. W.; Černy, R.; Hammer, B.; Jensen, T. R. The Mechanism of Mg 2+ Conduction in Ammine Magnesium Borohydride Promoted by a Neutral Molecule. *Phys. Chem. Chem. Phys.* **2020**, *22*, 9204−9209.
(55) Yan, Y.; Grinderslev, J. B.; Lee, Y. S.; Jørgensen, M.; Cho, Y. W.; Černý, R.; Jensen, T. R. Ammonia-Assisted fast Li-ion Conductivity in a new Hemiammine Lithium Borohydride, $LiBH_4 \cdot 1/2NH_3$. *Chem. Commun.* **2020**, *56*, 3971−3974.

https://doi.org/10.1021/acs.jpcc.2c04934
J. Phys. Chem. C 2022, 126, 15118−15127